Emergent Materials
https://doi.org/10.1007/s42247-023-00566-0

ORIGINAL ARTICLE

Morphology controlled fabrication of Fe_2O_3/GCN composites: a comparative study of hydrothermal and sonochemical synthesis methods for efficient sunlight driven photocatalysis for environmental remediation

Chetan Harak[1] · Dilip Satpute[1] · Vinayak Kadam[2] · Nitin Kolhe[1] · Anil Wade[1] · Shital Balgude[3] · Satish Mardikar[4] · Sagar Balgude[1] · Hari Pawar[1]

Received: 2 August 2023 / Accepted: 30 September 2023

Abstract
A novel bifunctional type of Z-scheme heterojunction with excellent adsorption and photocatalytic properties has been synthesized successfully using hydrothermal and sonochemical methods. The Fe_2O_3/g-C_3N_4 (GCN) nanocomposite, which has a distinct nanorod-like shape, has been characterized using various analytical techniques such as XRD, XPS, FESEM-EDS, TEM, and UV-DRS. The results of sunlight-driven photodegradation experiments indicate that the hydrothermally synthesized Fe_2O_3/GCN nanocomposite achieved a 95% degradation of methylene blue (MB) dye within 45 min. The improved photocatalytic activity is believed to be due to the formation of a *Z*-scheme heterojunction system, as supported by active species trapping experiments. Additionally, the composite photocatalyst demonstrated high degradation efficiency and stability over four cycles. Trapping studies c $^{\bullet}OH$ and $O_2^{\bullet-}$ were the principal active species in the photocatalytic process created by sunlight irradiation of a *Z*-scheme Fe_2O_3/GCN photocatalyst.

Keywords Heterojunction · Fe_2O_3/GCN · Graphitic carbon nitride · Photocatalysis

1 Introduction

Recently, visible-light active polymeric graphitic carbon nitride (GCN) with a narrow band gap of 2.7 eV has been reported as a novel metal-free photocatalyst [1]. GCN is a triazine-structured, metal-free semiconductor that is produced quickly by polymerizing inexpensive raw ingredients like thiourea, melamine, urea, and cyanamide [1]. Its exceptional physicochemical characteristics and use in a variety of applications, such as hydrogen production, carbon dioxide reduction, antibacterial activity, gas sensors, drug delivery, and photocatalysis, have sparked a significant deal of interest in the scientific community [2–6]. It is widely accepted that g-C_3N_4 is an excellent photocatalyst for the production of hydrogen and the degradation of hazardous organic pollutants. Organic pollutants discharged into the environment by industry are a major concern due to their high toxicity and potential health concerns to living beings [3]. Among the various approaches, semiconductor-based photocatalysis is considered as a highly effective technology for the degradation of organic dyes with utilization of solar energy [6]. The technology could mineralize a wide range of organic pollutants into low-toxic organic moieties, CO_2 and H_2O at mild temperatures and pressures without use of expensive oxidants. g-C_3N_4 has received a lot of attention due to its good band structure and potential for photocatalytic destruction of organic pollutants. Despite significant research on heterojunction photocatalysts made of semiconductors and g-C_3N_4, the high rate of photogenerated electron and hole recombination limits the application of g-C_3N_4 for the degradation of hazardous organic pollutants [7]. There are numerous reports on different heterojunction photocatalysts in the literature, such as CeO_2@g-C_3N_4, $ZnFe_2O_3$/g-C_3N_4, WO_3/g-C_3N_4,

✉ Sagar Balgude
sagarbalgude88@gmail.com

✉ Hari Pawar
haripawar2010@gmail.com

1 MES Abasaheb Garware College, Pune, Maharashtra, India

2 MGV'S Arts, Science and Commerce College, Nashik, Maharashtra, India

3 Shardabai Pawar Mahila Mahavidyalaya, Pune, Maharashtra, India

4 Smt. R S College, Sant Gadge Baba Amravati University, Amravati, Maharashtra, India

Published online: 18 October 2023

TiO_2/g-C_3N_4, Fe_2O_3/g-C_3N_4, and Bi_2O_3/g-C_3N_4 [8]. The Z-scheme heterojunction exhibits stronger oxidation and reduction abilities compared to those of single-component systems because of the more positive VB of one semiconductor and the more negative CB of another semiconductor [9]. Recently, enormous attention has been paid to the design and synthesis of g-C_3N_4-based Z-scheme photocatalysts to improve the activity of pristine g-C_3N_4. Compositing g-C_3N_4 with metal oxides results in a controlled band structure/band gap with enhanced visible light absorption and numerous active sites for photocatalytic reactions. For example, Zhao et al. successfully synthesized a g-C_3N_4/WO_3 heterojunction for the effective degradation of Rhodamine B dye under sunlight irradiation [9]. The synthesized heterojunctions were believed to channelize electrons from the conduction band of WO_3 to the valence band of g-C_3N_4, resulting in superior photocatalytic activity of the synthesized composites. In another report by Girish et al., g-C_3N_4 was composited with TiO_2, and they found that the photocatalytic efficiency of TiO_2 was significantly enhanced after making nanocomposites with g-C_3N_4 nanostructures [10]. Another Z-scheme photocatalyst composed of a g-C_3N_4/WS_2 heterojunction was reported by Nawaz et al. [11]. The composite catalyst was prepared by a one-pot hydrothermal fabrication method. The superior photoactivity was attributed to the p-n heterojunction formed due to the C_3N_4/WS_2 composite. In a report by Girish et al., a ZnO/g-C_3N_4 photocatalyst has been reported recently. The heterostructured photocatalyst was able to degrade dye as well as act as an HER catalyst [12]. The superior HER activity of the composite was ascribed to the increased charge-transfer rate owing to the better interfacial contact between the heterocomponents. The superior photoactivity was due to the nanoparticle nature of ZnO and g-C_3N_4 heterocomponents, which provided more exposed edge sites.

Magnetic metal oxide has recently gained popularity among researchers due to its ease of separation from the reaction mixture. Iron oxide (Fe_2O_3) is an important, nontoxic, abundant, low-cost material with narrow band gap [13]. The combination of Fe_2O_3 and g-C_3N_4 creates a heterojunction interface that effectively separates photogenerated electrons and holes [14]. These electron/hole pairs are crucial in photodegradation reactions. Several reports on the benefits of Fe_2O_3/g-C_3N_4 nanocomposite have been reported in the literature for various applications [8, 14–16]. These studies show that although significant progress has been made in improving the photocatalytic performance of Fe_2O_3/g-C_3N_4 nanocomposite, the photocatalytic performance still has to be improved. One efficient way to solve this problem is by morphologically modifying nanostructures, such as nanowires, nanosheets, nanorods, nanospheres, and nanoflowers, among others, with plenty of pores and large surface areas [17–19]. The objective of this study is to propose a template-free technique for creating tunable morphology Fe_2O_3/g-C_3N_4 nanocomposite materials by adjusting reaction conditions.

In present paper, sonochemical and hydrothermal methods were used for the synthesis of Fe_2O_3/g-C_3N_4 nanocomposites. The effect of synthesis parameters on nanocomposite growth was investigated, and as-synthesized samples were examined using different characterization techniques. The photocatalytic activity of as-synthesized nanocomposites under natural sunlight irradiation was evaluated using MB dye solution as a model hazardous organic pollutant. Using Fe_2O_3/g-C_3N_4 nanocomposites, the plausible mechanism for the degradation of MB dye solutions was also examined.

2 Experimental

2.1 Materials and methods

All of the chemicals used in this work were obtained from Merck and used without further purification. X-ray diffraction (XRD) measurements were carried out on a Philips diffractometer using Cu Kα radiation with a wavelength of 1.540 A^o at RT. The surface morphologies and microstructures of the Fe_2O_3/GCN nanocomposite were examined by the field emission scanning electron microscopy (JEOL JSM-7600F, FEG-SEM). X-ray photoelectron spectra were obtained using a Prevac specifically designed ambient pressure XPS system outfitted with a VG Scienta SAX 100 emission controller monochromator and an Al Ka anode (1486.6 eV) in transmission lens mode. The optical investigations were done using a Shimadzu UV-Vis spectrophotometer (Model 1800). The microstructure investigation of Fe_2O_3/GCN nanocomposite was performed using Transmission Electron Microscopy (JEOL JEM 2100 PLUS).

3 Synthesis of photocatalyst

Metal-free Graphitic carbon nitride ($_(GCN) was synthesized by a co-polymerization method. Melamine was used as the precursor in the process of copolymerization. Typically, a silica crucible containing 5 g of melamine was heated to 550 °C for 5 h at a rate of 2 °C/min. After cooling the silica crucible to room temperature naturally, the yellow powder was ground to produce g-C_3N_4. The acquired sample was lebelled as GCN and was further used to synthesize Fe_2O_3/GCN nanocomposites.

For the preparation of Fe_2O_3/GCN nanocomposite photocatalysts, a certain amount of iron (III) nitrate nonahydrate was first dissolved in 50 mL distilled water, and then 50 mg

GCN powder was dispersed in this solution by ultrasonication for 30 min. Subsequently, the pH of the above mixture was adjusted to 8–9 by dropwise adding of 0.2 M aqueous NaOH solution. The resultant mixture was treated sonochemically and hydrothermally independently after being magnetically agitated for 30 min at room temperature. For hydrothermal treatment, the reaction mixture was put into a 100-mL Teflon-lined stainless-steel autoclave, sealed, and kept at 140 °C for 24 h in oven. The autoclave was then allowed to cool naturally to ambient temperature. The precipitate was collected, centrifuged, washed, and dried in a 55 °C oven. The dry product was then calcinated for 4 h at 500 °C. The obtained sample was denoted as H-IGCN. Similarly, for sonochemical treatment, the magnetically stirred reaction mixture was exposed to ultrasonic probe radiation for 3 h (using a 5 s pulse ON and 2 s pulse OFF cycle with a 25% pulse amplitude). The precipitate was collected, centrifuged, washed and dried in a 55 °C oven. The dry product was then calcinated for 4 h at 500 °C. The obtained sample was denoted as S-IGCN.

4 Photodegradation and recycle experiments

The photocatalytic performance of as-synthesized Fe_2O_3/GCN composite photocatalysts was evaluated by the degradation of MB under sunlight irradiation. A 250-mL Pyrex beaker was used as the photoreactor. In a typical experiment, 0.1 g of catalyst was dispersed in a 100 mL, 10 mgL^{-1} aqueous solution of MB for 15 min using sonochemical bath. Prior to visible-light irradiation, the suspension was kept on magnetic stirring in the dark for an hour to establish adsorption-desorption equilibrium of MB on the catalyst surface at room temperature. After an hour, the suspension was exposed to the sunlight. During photodegradation experiments, at a regulated interval, 4 mL aliquot was collected on and then centrifuged to remove the catalyst particles for analysis. The residual MB concentration during photodegradation was monitored using a UV-Vis spectrophotometer by measuring its light absorbance at 664 nm. After the photodegradation process, the nanocomposites were separated from the solution using a centrifuge operating at 3000 rpm for 20 min. Subsequently, they were thoroughly washed to eliminate any remaining MB residue adhered to the Fe_2O_3/GCN surface. These nanocomposites were then dried in an oven at 100 °C for 2 h, resulting in a powdered form. This recovered catalyst powder was employed in a reusability experiment following the same photocatalytic method. This experiment was repeated for the first, second, and third cycles. To investigate the active species generated during the photocatalytic reaction, including holes (h^+), hydroxyl (OH•) radicals, and superoxide ion ($O_2^{\bullet-}$) radicals, 1 mmol L^{-1} of ethylene diamine tetraacetic acid (EDTA), isopropanol (IPA), and benzoquinone (BQ) were introduced into the MB dye solution.

5 Results and discussion

The morphological investigation of GCN, S-IGCN, and H-IGCN composites was performed using field emission scanning electron microscopy (FE-SEM). Figure 1 depicts FESEM images of as-synthesized GCN, S-IGCN, and H-IGCN composites, respectively. It can be observed from Figure 1a, b that bare GCN exhibits a typical layered structure with wrinkles. Figure 1d, e shows FESEM images of an S-IGCN composite fabricated by sonochemical treatment. The high magnification image (Figure 1d) reveals the formation of unevenly shaped crystals with variable size. Figure 1e shows that these unevenly shaped nanoparticles are aggregated on the surface of graphitic carbon nitride. Similarly, the formation of nanorods on the surface of graphitic carbon nitride produced during hydrothermal treatment can be observed in the case of H-IGCN composite (Figure 1g). A close examination of these composites reveals the nanorod-like shape of the as-produced H-IGCN composite (Figure 1h). These uniformly developed nanorods exhibits a diameter in the range of 10–20 nm and a length ~20–60 nm. It is evident from Figure 1 that the fabrication method has a considerable impact on the morphology evolution of the Fe_2O_3/GCN nanocomposite and plays a key role in its growth. Furthermore, corresponding EDS elemental mapping of as-synthesized GCN, S-IGCN, and H-IGCN composites are depicted in Figure 1c, f, i, respectively. The results are in close agreement with the synthetic architecture utilized for synthesis of bare GCN and composites of GCN with Fe_2O_3 viz. S-IGCN and H-IGCN.

The investigation of the microstructure of a H-IGCN nanocomposite was conducted using transmission electron microscopy (TEM), as depicted in Figure 2. This revealed the presence of nanorod-like morphology of H-IGCN nanocomposite (Figure 2a, b), which is good agreement with FESEM results (Figure 1g, h). The inset of Figure 2c displays lattice fringes with a spacing of 0.37 nm, corresponding to the (012) lattice plane of Fe_2O_3. The selected area electron diffraction (SAED) pattern of the H-IGCN nanocomposite, as shown in Figure 2d, clearly indicates its crystalline nature.

The X-ray diffraction patterns for the as-synthesized GCN, S-IGCN, and H-IGCN composites are shown in Figure 3. As can be seen from Figure 3a, the XRD peaks for bare GCN appearing at 27.4° corresponds to the (002) stacking layered structure. These results are in accordance with JCPDS card No. 87-1526 [20]. Furthermore, the XRD patterns of S-IGCN and H–IGCN composites are depicted

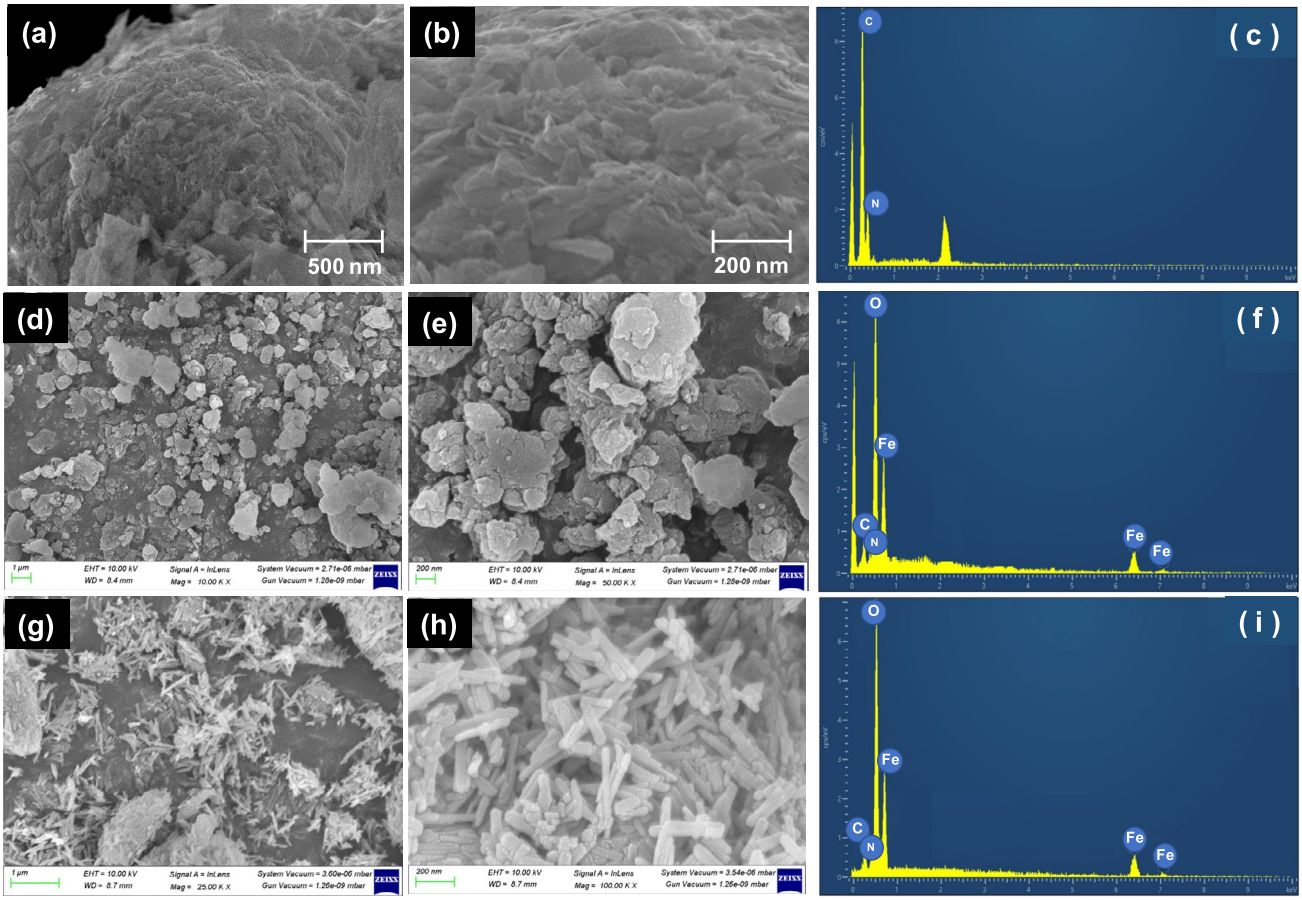

Fig. 1 FESEM images of GCN, S-IGCN, and H-IGCN (**a**, **b**, **d**, **e**, **g**, **h**) along with their corresponding EDS elemental mapping (**c**, **f**, **i**)

in Figure 3b. For H-IGCN, the diffraction peaks appearing at 23.98°, 29.99°, 33.03°, 35.50°, 40.78°, 49.27°, 53.93°, 57.35°, 62.28°, 63.81°, and 71.66° corresponds to (012), (002), (104), (110), (113), (024), (116), (122), (214), (030), and (220) planes. The presence of Fe_2O_3 and GCN peaks in the H-IGCN composites demonstrates that Fe_2O_3 was uniformly integrated onto crystalline GCN surface [13]. A similar XRD pattern was observed for the S-IGCN sample, with higher peak intensity than the H-IGCN sample. In both the composites, besides diffraction peaks of GCN and Fe_2O_3, no diffraction peaks related to any impurities were observed, indicating the formation of highly pure Fe_2O_3/GCN nanocomposites.

We also looked at the optical characteristics of the as-synthesized GCN, S-IGCN, and H-IGCN composites. The UV-vis diffuse reflectance spectra of bare GCN and the composite catalysts were recorded between 200 and 800 nm and are depicted in Figure 4a. From figure it can be seen that the bare GCN shows an absorption edge at about 433 nm. Furthermore, it is remarkable that the absorption curves of S-IGCN and H-IGCN composites are similar to bare GCN with higher intensity and shifted towards longer wavelength. The optical spectra of S-IGCN shows absorption edge at ~551.86 nm, which is typically reported in the literature [21], whereas the H-IGCN displays a potent absorption band at ~590.68 nm. Meanwhile, the colors of the composites change from yellow for bare GCN to crimson and maroon for S-IGCN and H–IGCN, respectively, indicating the modification of the optical properties of Fe_2O_3/GCN composites. The representative schematic pertaining to color change of bare GCN after compositing with Fe_2O_3 via individual hydrothermal and sonochemical processing in present investigation is depicted in Figure 5.

Furthermore, the UV-vis diffused reflectance data was used to calculate band gap energies of composite photocatalysts by using the following equation and the results are depicted in Figure 4b:

$$\alpha hv = A(hv - Eg)^{n/2} \quad (1)$$

where α, h, v, A, and E_g represent the absorption coefficient, Planck constant, light frequency, proportionality constant, and band gap energy, respectively. The value of n is determined from the nature of optical transition. $n=2$

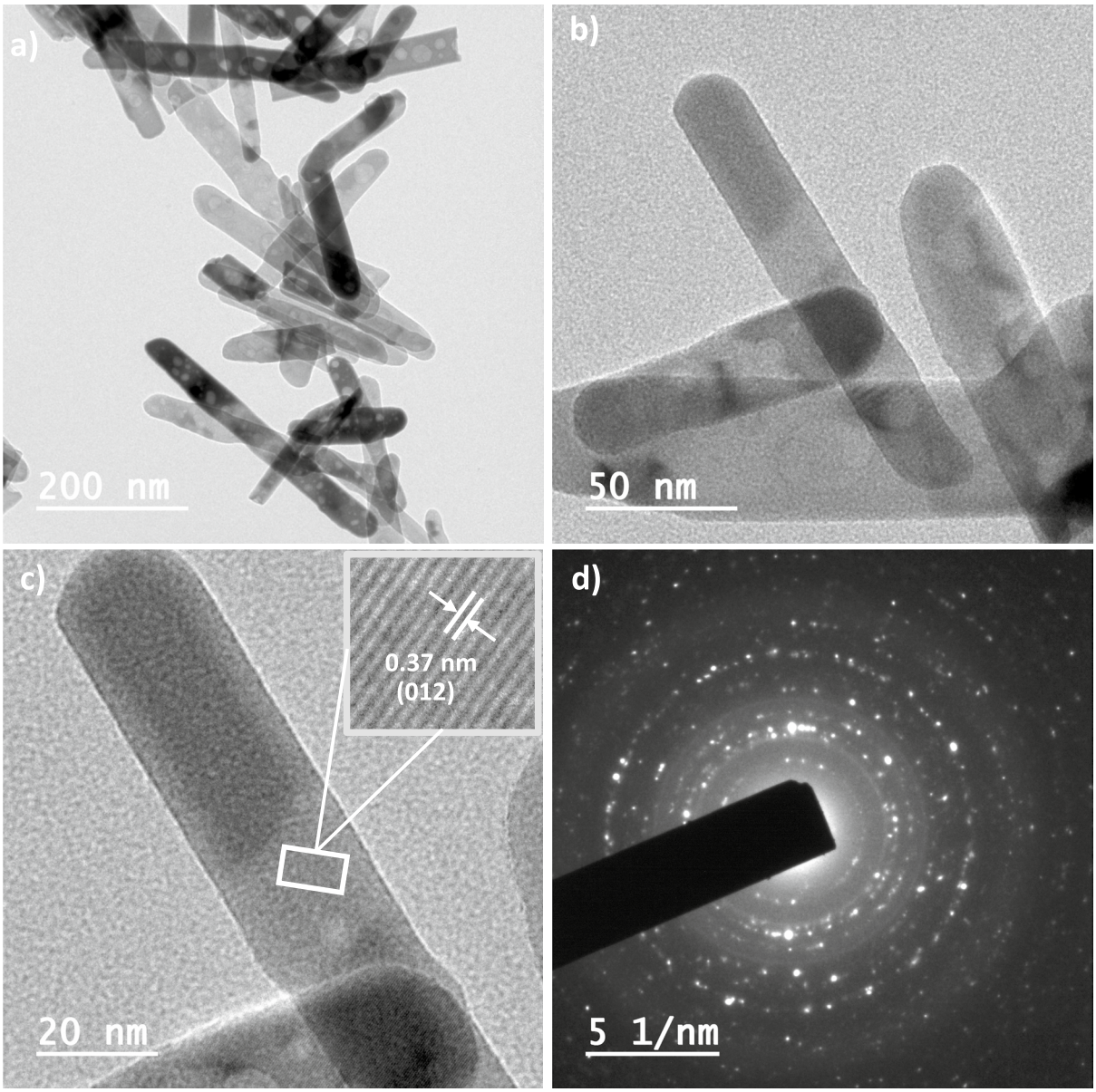

Fig. 2 **a**, **b** & **c** TEM images and **d** SAED pattern of H-IGCN

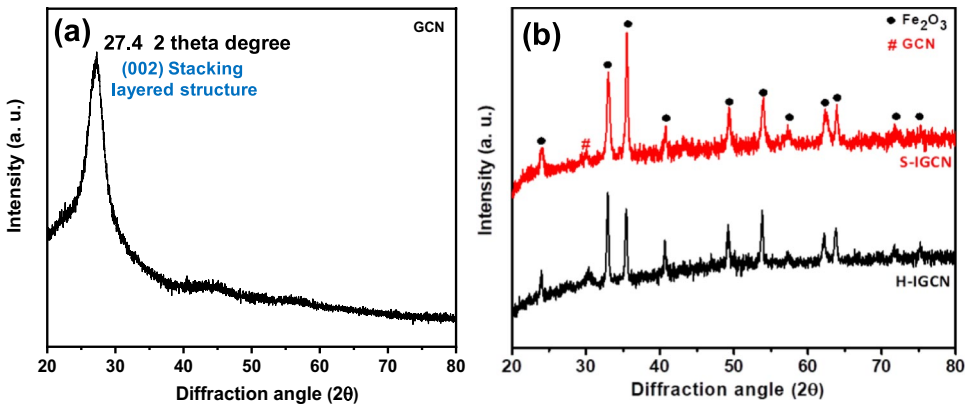

Fig. 3 XRD pattern of as-synthesized **a** GCN and **b** Fe_2O_3/GCN composites, respectively

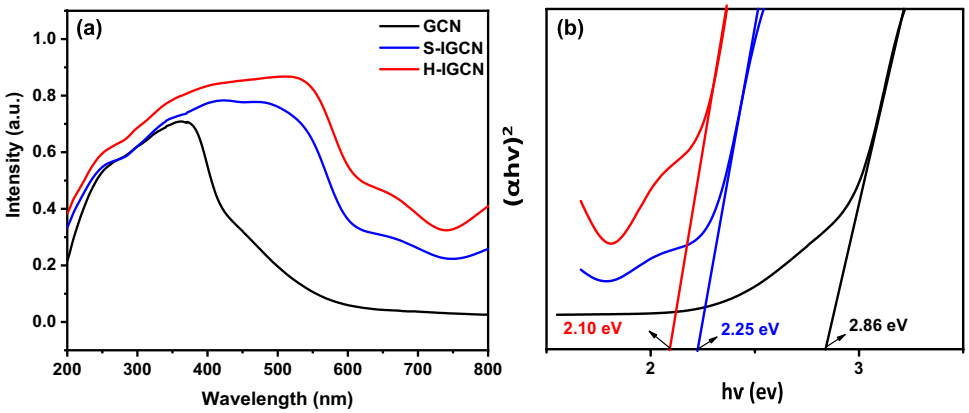

Fig. 4 **a** UV–vis diffuse reflectance spectra of GCN, S-IGCN, and H-IGCN composite photocatalysts. **b** Plot of $(\alpha h\nu)^2$ vs. photon energy ($h\nu$) for GCN, S-IGCN, and H-IGCN composite photocatalysts

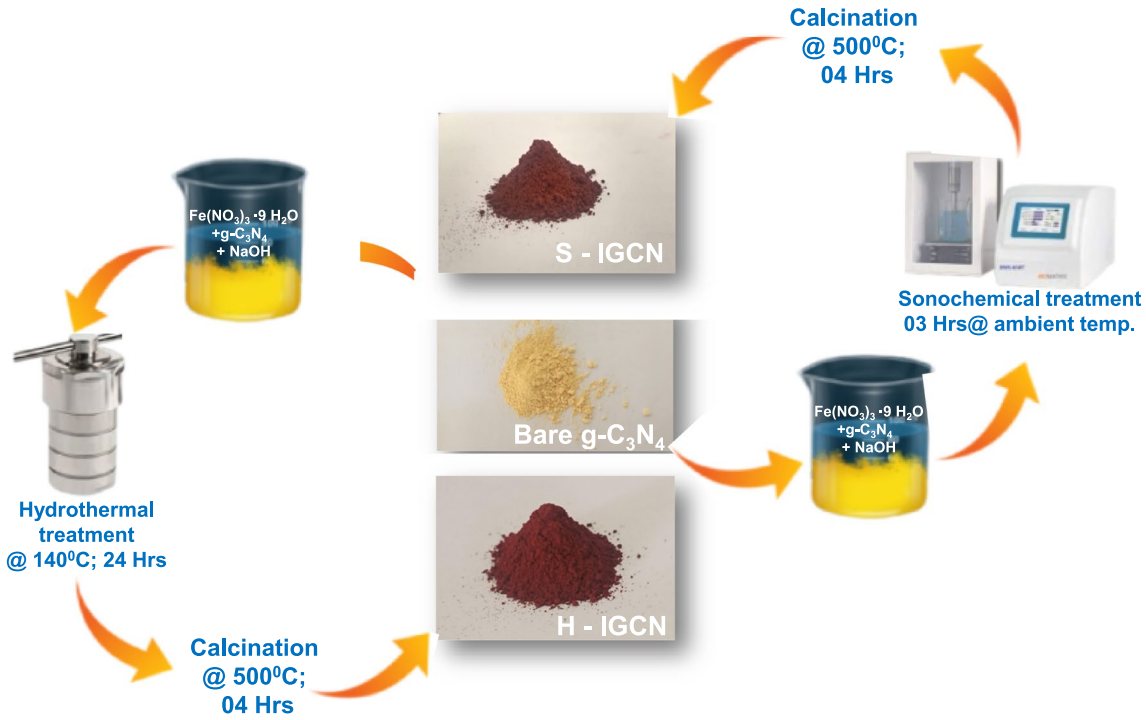

Fig. 5 Representative schematic illustrating color change of bare GCN after compositing with Fe_2O_3 via individual hydrothermal and sonochemical processing in present investigation

or 3 for indirect allowed and indirect forbidden transition, respectively, and $n = 1/2$ or 3/2 for direct allowed and direct forbidden transition, respectively. The calculated band gaps for the GCN, S-IGCN, and H-IGCN composites were found to be 2.86, 2.25 eV, and 2.10 eV, respectively. In the case of H-IGCN composite compared to S-IGCN, the band gap was seen to be narrowing. This band gap narrowing may be attributed to nanorods-like morphology of H-IGCN [17]. When H-IGCN are exposed to sunlight, 1D hierarchical nanostructures that resemble nanorods cause light dispersion, which increases light harvesting compared to S-IGCN nanostructures. This could be advantageous for the photocatalytic activity of H-IGCN [22].

The chemical binding state of each atom in H-IGCN was confirmed by X-ray photoelectron spectroscopy. The high-resolution spectra of C, N, Fe, and O elements were depicted in Figure 6. The high-resolution spectra of C 1s show two primary peaks in Figure 6a, at 288.86 and 285.05 eV, which were attributed to C-$(N)_3$ and C-C bonding in the GCN lattice, respectively [23]. The peak observed at 286.62 eV could be the result of SP^2 hybridized carbon atoms present in C=N, which could be detected by graphitic domains in a CN matrix [24]. The high-resolution spectra of N 1s of the H-IGCN were deconvoluted in the peaks at 398.67, 399.30, and 400.21 eV, which were assigned to C-N-C, N-C_3, and C-N-H groups in the triazine rings of GCN (Figure 6b) [25].

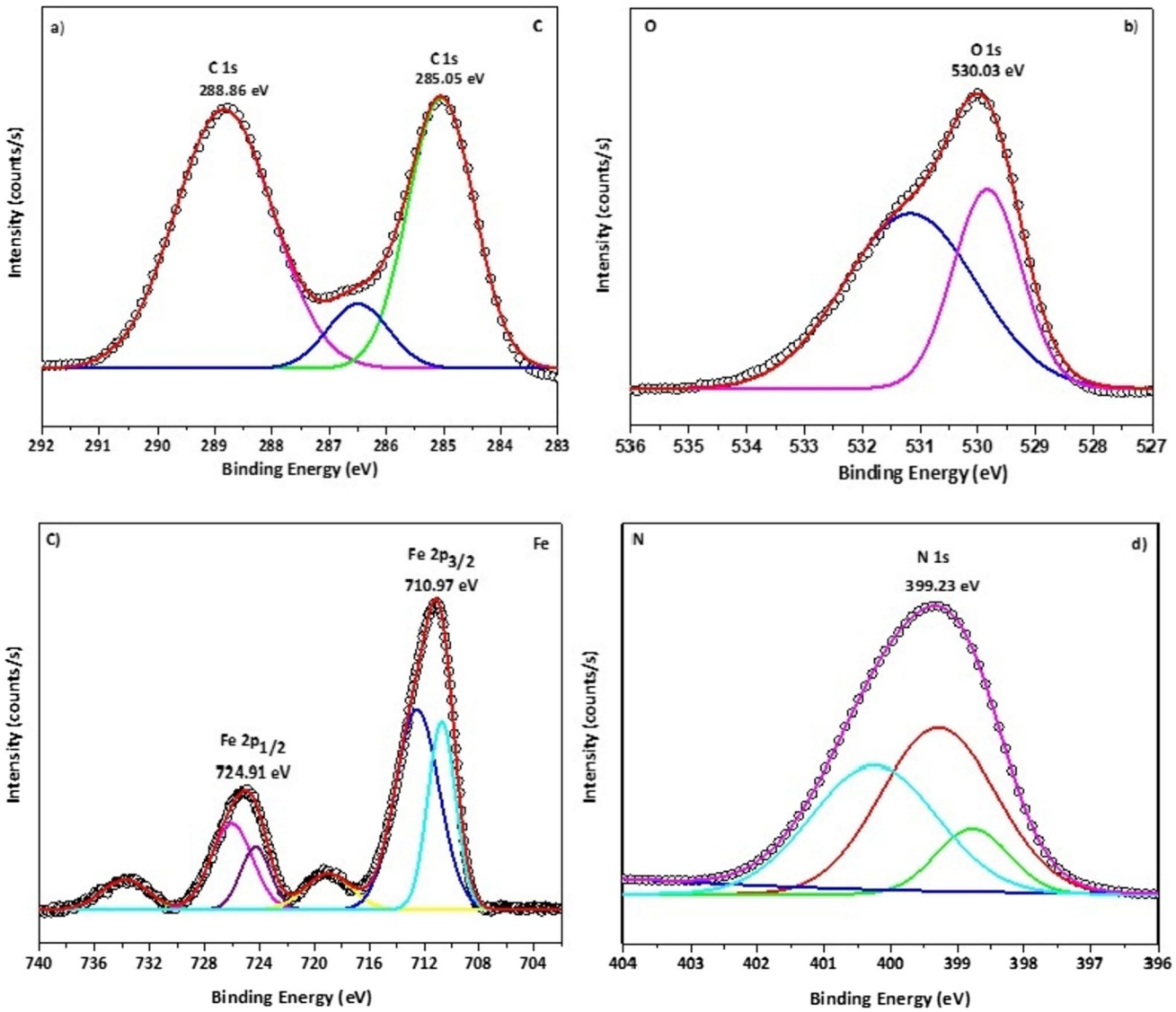

Fig. 6 High resolution XPS spectra of **a** C 1s, **b** O 1s, **c** Fe 2p, and **d** N 1s for representative H-IGCN composite

High-resolution spectra of the Fe 2p in H-IGCN are shown in Figure 6c, with the characteristic peaks of Fe $2p_{3/2}$ and Fe $2p_{1/2}$ being seen at binding energies of 710.97 and 724.91 eV, respectively [26]. There are two satellite peaks for Fe^{3+} in the H-IGCN, located at 719.23 and 733.45 eV. The characteristic peaks of O 1s were observed at 530.03 eV of binding energy (Figure 6d), which could be deconvoluted into two peaks. The Fe-O binding energy of Fe_2O_3 is shown by the peak at 529.36 eV, whereas the carbon-oxygen binding energy is represented by the peak at 531.25 eV [24]. In the comprehensive XPS investigation, no impurity peak was identified, indicating the formation of a highly pure Fe_2O_3/GCN composite.

The photocatalytic activity of as-synthesized H-IGCN and S-IGCN for the methylene blue degradation of the model textile dye was evaluated in the presence of sunlight irradiation. Figure 7a depicts the absorption of aqueous MB dye under various testing conditions and time periods. The graph demonstrates that in the presence of the photocatalysts, the absorbance of aqueous solutions of MB dye declined steadily as the illumination time increased. The pure GCN exhibits a poorer response to MB dye degradation compared to Fe_2O_3/g-C_3N_4 composites. The H-IGCN photocatalyst degraded more than 95% of the MB dye after 45 min, compared to 84% for the S-IGCN photocatalyst during the same time period. The fact that the rate of MB dye degradation was observed to be higher in case of H-IGCN compared to S-IGCN clearly demonstrates that band structure and nanorod-like morphology have a significant impact on the efficiency of MB dye degradation under the comparable

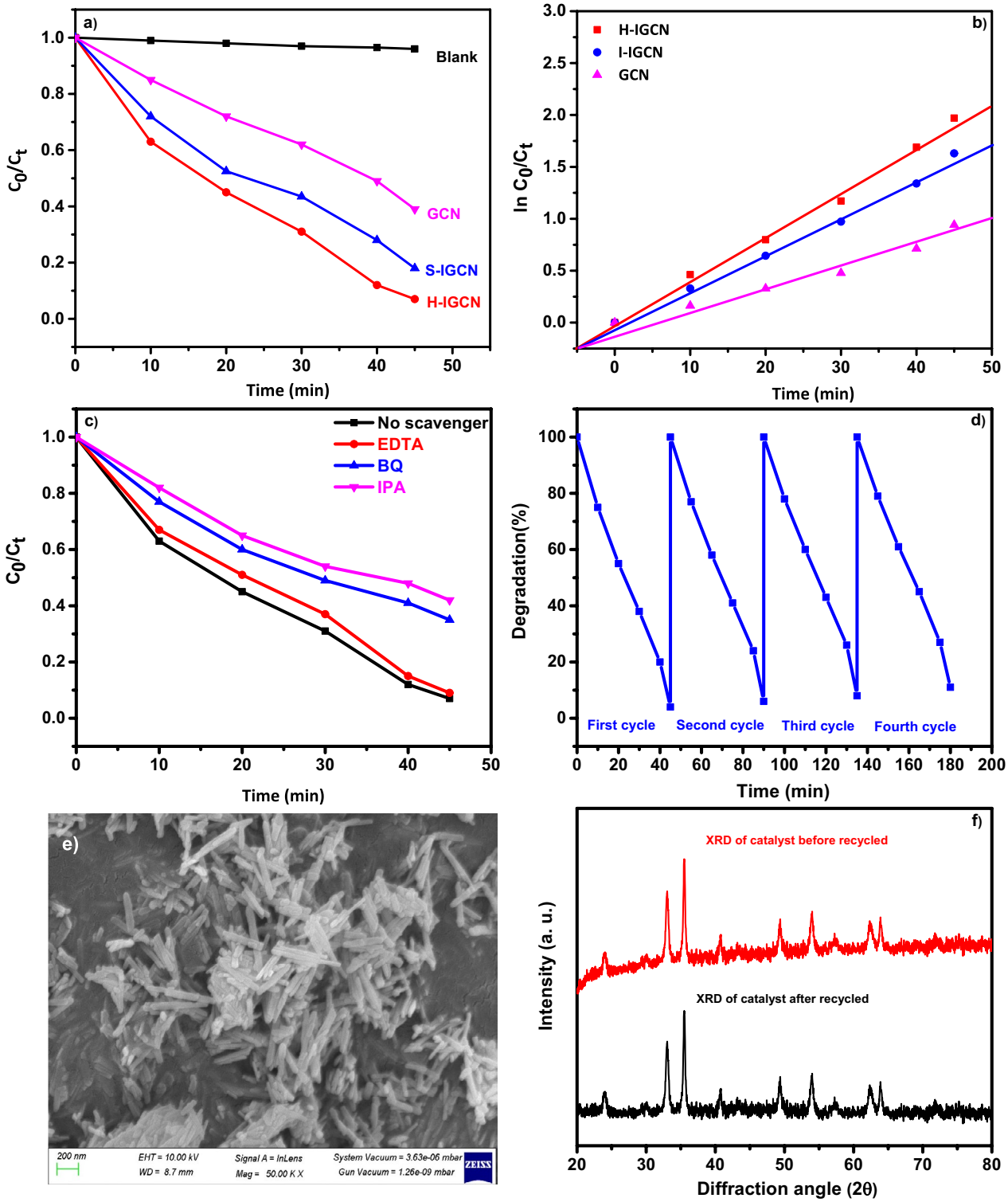

Fig. 7 **a** Photocatalytic degradation of MB dye in aqueous solution using GCN, H-IGCN, and S-IGCN composites; **b** plot of $\ln(C_0/C_t)$ vs. reaction time for the photocatalytic MB degradation using GCN, H-IGCN, and S-IGCN composites; **c** effect of scavengers on MB degradation over H-IGCN composite; **d** recyclability for photodegradation of MB dye by H-IGCN; **e** FESEM of H-IGCN after photocatalytic reaction; and **f** XRD spectra of H-IGCN before and after photocatalytic reaction

conditions. For comparison, a controlled experiment was also conducted without a catalyst. The MB dye scarcely decomposed in the absence of a catalyst. Therefore, exposure to light has a significant impact on the degradation of aqueous MB dye.

In addition, the kinetics of the reactions of the GCN, H-IGCN, and S-IGCN photocatalysts in the degradation of MB were studied. Figure 7b depicts pseudo first-order kinetic graphs of $\ln(C_0/C_t)$ vs. time for MB degradation. The rate constants for the GCN, H-IGCN, and S-IGCN composites were found to be 0.0123, 0.0178, and 0.0163 min^{-1}, respectively. The results suggest that under identical conditions, the H-IGCN composite should have superior photocatalytic activity than the S-IGCN composite. The comparative results of MB dye degradation are shown in Table 1 [12, 27–31]. The highest degradation of methylene blue (MB) was successfully accomplished using H-IGCN, primarily owing to its narrow band gap and the presence of a well-defined crystalline nanorod-like structure. The narrow band gap falls within the visible spectrum, allowing for the absorption of a maximal amount of sunlight and thereby generating the highest number of electron-hole pairs. These findings unambiguously show that morphologically controlled synthesis of Fe_2O_3 with g-C_3N_4 considerably improves photocatalytic activity [32].

The contribution of various active radicals to the degradation of MB dye using the H-IGCN photocatalyst has been examined using radical trapping studies. To capture holes, hydroxyl radicals, and superoxide radicals in radical trapping assays, 1 mmol of ethylenediaminetetraacetic acid (EDTA), isopropanol (IPA), and Benzoquinone (BQ) are introduced to the photocatalytic system [33]. Figure 7c depicts the photocatalytic activity of H-IGCN in the presence of several trapping agents. Form figure, the results demonstrate that the photocatalytic activity of the H-IGCN nanocomposite was significantly reduced in the presence of IPA and BQ, indicating that the principal oxidative species involved in the degradation process are $^{\bullet}OH$ and $O_2^{\bullet-}$. The photocatalytic activity is unaffected by the addition of EDTA to trap h^+, proving that holes are not the main active species in the system at hand. The obtained results demonstrated that the rate of MB dye degradation is significantly influenced by the concentration of hydroxyl and superoxide radicals.

The reusability investigation of the photodegradation of MB dye utilizing H-IGCN composite is shown in Figure 7d. Figure shows that the performance of the H-IGCN composite remained consistent after four cycles with very little performance variation caused by catalyst loss during handling. These results revealed that the H-IGCN composite was a stable and effective photocatalyst when compared to previously published reports [33–36]. Following four cycles, the catalyst demonstrates nearly identical degradation effectiveness. Figure 7e displays the FESEM image of the photocatalyst after recovery, revealing a structure similar to that shown in Figure 1. This observation underscores the photocatalyst's excellent stability, further confirming its suitability for extended use. Furthermore, the crystal structure of H-IGCN remains unchanged throughout the photocatalytic degradation reactions (as shown in Figure 7f), suggesting that H-IGCN is a reliable catalyst activated by sunlight and therefore well-suited for practical uses in the industry.

On the basis of the above explanation, a probable mechanism for MB photocatalytic degradation employing the H-IGCN composite under sunlight illumination can be proposed. Figure 8 shows the possible mechanism of photodegradation of MB dye in the presence of H-IGCN (Fe_2O_3/GCN) nanocomposite. The charge transfer mechanism between the interfacial phase could be regulated by the *Z*-scheme [37]. After sunlight is irradiated on the surface of the photocatalyst, electron and hole pairs are formed. These photogenerated e^-/h^+ pairs are responsible for photodegradation of MB dye. The h^+ in VB of Fe_2O_3 react with H_2O molecule to generate radicals. While electrons in the CB of Fe_2O_3 migrate to the VB of GCN, this mechanism is advantageous for separating e^-/h^+ pairs on different sides of the Fe_2O_3/GCN composite. The transferred electron in the CB of GCN can easily convert O_2 to $O_2^{\bullet-}$ radical. The radical scavenger experiment provided evidence for the generation of $^{\bullet}OH$ and $O_2^{\bullet-}$ active radicals (Fig. 7c). These photogenerated active hydroxyl/superoxide radicals can then cause the degradation of the MB dye molecule [22].

Table 1 Comparison of photocatalytic MB dye degradation with some other photocatalysts

Photocatalysts	Light source	Dye concentration	Amount of catalyst (g/L)	Time (min)	% degradation	References
ZnO@g-C_3N_4	250 W Xenon lamp	5 ppm	0.4	120	91.5%	[12]
P25	Sunlight	10 ppm	0.5	70	94%	[27]
g-C_3N_4@ TiO_2	Solar light	10 ppm	0.02	100	94.92%	[28]
$CdMoO_4$@g-C_3N_4	35 W Xenon arc lamp	10 ppm	0.01	145	93.70%	[29]
g-C_3N_4@ MoS_2	Sunlight	5 ppm	0.1	80	98.7%	[30]
WO_3@g-C_3N_4	Visible light	50 ppm	0.5	90	95%	[31]
Fe_2O_3/g-C_3N_4	Sunlight	10 ppm	0.1	45	95%	Present work

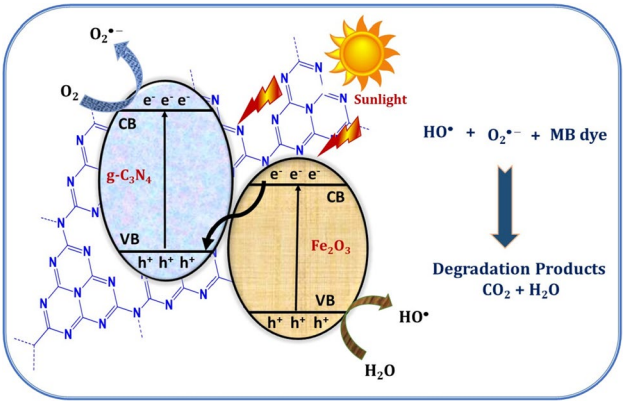

Fig. 8 Possible mechanism of photodegradation of MB dye in the presence of H-IGCN (Fe_2O_3/GCN) nanocomposite

6 Conclusion

In conclusion, a very effective Fe_2O_3/GCN composite that was made utilizing several synthesis techniques has been a fascinating way to examine the impact of synthesis technique on various properties of a single nanocomposite. The phase structure, morphology, and optical properties of Fe_2O_3/GCN composites have been thoroughly studied. The photocatalytic activity of as-synthesized Fe_2O_3/GCN for MB dye degradation was high. The increased photocatalytic activity of a nanorods-like Fe_2O_3/GCN composite was attributed to morphology, the synergistic effects of Fe_2O_3 loading on the surface of GCN, and separation of photoexcited electron-hole carriers.

Acknowledgements The authors are grateful to Dr. P. B. Buchade, principal of the MES Abasaheb Garware College in Pune, and Dr. Shobha A. Waghmode, head of the chemistry department, for their support and encouragement. HRP is grateful to the Maharashtra Education Society in Pune for providing research facilities.

Author contribution CH: methodology, conceptualization. DS: validation, methodology. VK: resources, data curation, writing—review and editing. NK: investigation, validation. AW: formal analysis, data curation, validation. SB: visualization, formal analysis. SM: data curation, software, writing—review and editing. SB: writing—original draft, writing—review and editing. HP: supervision, resources.

Declarations

Competing interests The authors declare no competing interests.

Statement of industrial relevance The successful synthesis of the Fe_2O_3/GCN nanocomposite with excellent adsorption and photocatalytic properties holds significant industrial relevance in the field of wastewater treatment and environmental remediation. The high degradation efficiency and stability of the composite photocatalyst, along with its ability to effectively degrade organic dyes under sunlight irradiation, make it a promising candidate for the development of advanced photocatalytic systems for industrial applications.

Statement of novelty The novel bifunctional Z-scheme heterojunction synthesized through hydrothermal and sonochemical methods represents a significant advancement in the field of photocatalysis. The distinct nanorod-like shape of the Fe_2O_3/GCN nanocomposite, along with its characterization using various analytical techniques, highlights the meticulous research and comprehensive understanding of the material's properties. The formation of a Z-scheme heterojunction system and the identification of $^{\bullet}OH$ and $O_2^{\bullet-}$ as the principal active species through trapping studies demonstrate a novel approach to enhancing photocatalytic activity. The achievement of 95% degradation of methylene blue dye within a short duration further emphasizes the novelty and practical applicability of this nanocomposite.

References

1. V.V. Pham, T.K. Truong, L.V. Hai, H.P.P. La, H.T. Nguyen, V.Q. Lam, H.D. Tong, T.Q. Nguyen, A. Sabbah, K.-H. Chen, S.-J. You, T.M. Cao, S-Scheme α-Fe2O3/g-C3N4 nanocomposites as heterojunction photocatalysts for antibiotic degradation. ACS Appl. Nano Mater. **5**, 4506–4514 (2022)
2. G. Zhang, D. Huang, M. Cheng, L. Lei, S. Chen, R. Wang, W. Xue, Y. Liu, Y. Chen, Z. Li, Megamerger of MOFs and gC 3 N 4 for energy and environment applications: Upgrading the framework stability and performance. J. Mater. Chem. A **8**, 17883–17906 (2020)
3. J. Wen, J. Xie, X. Chen, X. Li, A review on g-C3N4-based photocatalysts. Appl. Surf. Sci. **391**, 72–123 (2017)
4. N. Rahman, J. Yang, M. Zulfiqar, R. Sohail, A. Khan, C. Iqbal, A.A. Maouche, M. Khan, S.A. Husain, S.N. Khattak, A. Khan. Khan, Insight into metallic oxide semiconductor (SnO2, ZnO, CuO, α-Fe2O3, WO3)-carbon nitride (g-C3N4) heterojunction for gas sensing application. Sensors and Actuators A: Physical **332**, 113128 (2021)
5. Z. Zhao, Y. Sun, F. Dong, Graphitic carbon nitride based nanocomposites: a review. Nanoscale **7**(1), 15–37 (2015)
6. S. Balgude, S. Barkade, S. Mardikar, *Metal oxides for high-performance hydrogen generation by water splitting*, Multifunctional nanostructured metal oxides for energy harvesting and storage devices, 169–194 (2020)
7. L. Wang, K. Wang, T. He, Y. Zhao, H. Song, H. Wang, Graphitic carbon nitride-based photocatalytic materials: preparation strategy and application. ACS Sustain. Chem. Eng. **8**, 16048–16085 (2020)
8. Y. Zhang, J. Yuan, Y. Ding, B. Liu, L. Zhao, S. Zhang, Research progress on g–C3N4–based photocatalysts for organic pollutants degradation in wastewater: From exciton and carrier perspectives. Ceram. Int. **47**, 31005–31030 (2021)
9. Q. Zhao, S. Liu, S. Chen, B. Ren, Y. Zhang, X. Luo, Y. Sun, Facile ball-milling synthesis of WO3/g-C3N4 heterojunction for photocatalytic degradation of Rhodamine B. Chem. Phys. Lett. **805**, 139908 (2022)
10. Y.R. Girish, G. Udayabhanu, A. Alnaggar, M.B. Hezam, G. Nayan, K. Byrappa. Nagaraju, Facile and rapid synthesis of solar-driven TiO2/g-C3N4 heterostructure photocatalysts for enhanced photocatalytic activity. J. Sci: Adv. Mater. Dev. **7**, 100419 (2022)
11. A. Nawaz, S. Goudarzi, P. Saravanan, H. Zarrin, Z-scheme induced g-C3N4/WS2 heterojunction photocatalyst with improved electron mobility for enhanced solar photocatalysis. Sol. Energy **228**, 53–67 (2021)
12. Y.R. Girish, N.M. Udayabhanu, G. Byrappa, A. Alnaggar, G. Hezam, K. Nagaraju, K. Byrappa. Pramoda, Rapid and facile

synthesis of Z-scheme ZnO/g-C3N4 heterostructure as efficient visible light-driven photocatalysts for dye degradation and hydrogen evolution reaction. J. Hazard. Mater. Adv. **9**, 100230 (2023)
13. S. Balgude, S. Godase, A. Shinde, C. Harak, Succinate assisted synthesis of magnetically separable Fe2O3/g-C3N4 nano-heterostructure: A stable catalyst for environmental remediation. Current Res. Green Sustain. Chem. **4**, 100210 (2021)
14. B.P. Mishra, K. Parida, Orienting Z scheme charge transfer in graphitic carbon nitride-based systems for photocatalytic energy and environmental applications. J. Mater. Chem. A **9**, 10039–10080 (2021)
15. J. Xing, N. Wang, X. Li, J. Wang, M. Taiwaikuli, X. Huang, T. Wang, L. Zhou, H. Hao, Synthesis and modifications of g-C3N4-based materials and their applications in wastewater pollutants removal. J. Environ. Chem. Eng. **10**, 108782 (2022)
16. P. Gan, Z. Zhang, Y. Hu, Y. Li, J. Ye, M. Tong, J. Liang, Insight into the role of Fe in the synergetic effect of persulfate/sulfite and Fe2O3@ g-C3N4 for carbamazepine degradation. Sci. Total Environ. **819**, 152787 (2022)
17. P. Mone, S. Mardikar, S. Balgude, Morphology-controlled synthesis of Sn3O4 nanowires for enhanced solar-light driven photocatalytic H2 production. Nano-Structures & Nano-Objects **24**, 100615 (2020)
18. Y. Wang, X. Xiao, M. Lu, Y. Xiao, 3D network-like rGO-MoSe2 modified g-C3N4 nanosheets with Z-scheme heterojunction: Morphology control, heterojunction construct, and boosted photocatalytic performances. J. Alloy. Compd. **897**, 163197 (2022)
19. H. Dong, X. Zhang, J. Li, P. Zhou, S. Yu, N. Song, C. Liu, G. Che, C. Li, Construction of morphology-controlled nonmetal 2D/3D homojunction towards enhancing photocatalytic activity and mechanism insight. Appl. Catal. B **263**, 118270 (2020)
20. K. Hu, P. Liu, Z. Zhang, J. Bian, G. Wang, H. Wu, H. Xu, L. Jing, Improved photocatalytic activities of g-C3N4 nanosheets by B doping and Ru-Oxo cluster modification for CO2 conversion. J. Phys. Chem. C **126**, 9704–9712 (2022)
21. D. Xiao, K. Dai, Y. Qu, Y. Yin, H. Chen, Hydrothermal synthesis of α-Fe2O3/g-C3N4 composite and its efficient photocatalytic reduction of Cr (VI) under visible light. Appl. Surf. Sci. **358**, 181–187 (2015)
22. K. Jangam, S. Balgude, H. Pawar, S. Patange, P. More, Effect of cobalt substitution in Zn1-xCoxFeCrO4 ferri-chromate: emerging light absorber for degradation of model textile dye. Surfaces and Interfaces **33**, 102189 (2022)
23. L. Zhang, C. Liu, Q. Wang, X. Wang, S. Wang, Electrochemical sensor based on an electrode modified with porous graphitic carbon nitride nanosheets (C3N4) embedded in graphene oxide for simultaneous determination of ascorbic acid, dopamine and uric acid. Microchim. Acta **187**, 149 (2020)
24. S. Vignesh, S. Suganthi, J. KalyanaSundar, V. Raj, Construction of α-Fe2O3/CeO2 decorated g-C3N4 nanosheets for magnetically separable efficient photocatalytic performance under visible light exposure and bacterial disinfection. Appl Surf Sci **488**, 763–777 (2019)
25. W. An, L. Tian, J. Hu, L. Liu, W. Cui, Y. Liang, Efficient degradation of organic pollutants by catalytic ozonation and photocatalysis synergy system using double-functional MgO/g-C3N4 catalyst. Appl. Surf. Sci. **534**, 147518 (2020)
26. M.J. Kang, H. Yu, W. Lee, H.G. Cha, Efficient Fe2O3/Cg-C3N4 Z-scheme heterojunction photocatalyst prepared by facile one-step carbonizing process. J. Phys. Chem. Solids **130**, 93–99 (2019)
27. S. Balgude, Y. Sethi, A. Gaikwad, B. Kale, D. Amalnerkar, P. Adhyapak, Nanoscale **12**, 8502–8510 (2020)
28. M.H. Barzegar, M.M. Sabzehmeidani, M. Ghaedi, V.M. Avargani, Z. Moradi, V.A.L. Roy, H. Heidari, S-scheme heterojunction g-C3N4/TiO2 with enhanced photocatalytic activity for degradation of a binary mixture of cationic dyes using solar parabolic trough reactor. Chem. Eng. Res. Des. **174**, 307–318 (2021)
29. A. Gandamalla, S. Manchala, P. Anand, Y.-P. Fu, V. Shanker, Development of versatile CdMoO4/g-C3N4 nanocomposite for enhanced photoelectrochemical oxygen evolution reaction and photocatalytic dye degradation applications. Materials Today Chemistry **19**, 100392 (2021)
30. Y. He, Z. Ma, L.B. Junior, Distinctive binary g-C3N4/MoS2 heterojunctions with highly efficient ultrasonic catalytic degradation for levofloxacin and methylene blue. Ceram. Int. **46**, 12364–12372 (2020)
31. X. Liu, A. Jin, Y. Jia, T. Xia, C. Deng, M. Zhu, C. Chen, X. Chen, Synergy of adsorption and visible-light photocatalytic degradation of methylene blue by a bifunctional Z-scheme heterojunction of WO3/g-C3N4. Appl. Surf. Sci. **405**, 359–371 (2017)
32. X. Shu, J. Zhou, W. Lian, Y. Jiang, Y. Wang, R. Shu, Y. Liu, J. Han, Y. Zhuang, Size-morphology control, surface reaction mechanism and excellent electromagnetic wave absorption characteristics of Fe3O4 hollow spheres. J. Alloy. Compd. **854**, 157087 (2021)
33. M. Jourshabani, Z. Shariatinia, A. Badiei, High efficiency visible-light-driven Fe2O3-xSx/S-doped g-C3N4 heterojunction photocatalysts: direct Z-scheme mechanism. J. Mater. Sci. Technol. **34**, 1511–1525 (2018)
34. D. Monga, D. Ilager, N.P. Shetti, S. Basu, T.M. Aminabhavi, 2D/2d heterojunction of MoS2/g-C3N4 nanoflowers for enhanced visible-light-driven photocatalytic and electrochemical degradation of organic pollutants. J. Environ. Manage. **274**, 111208 (2020)
35. R. Uma, K. Ravichandran, S. Sriram, B. Sakthivel, Cost-effective fabrication of ZnO/g-C3N4 composite thin films for enhanced photocatalytic activity against three different dyes (MB, MG and RhB). Mater. Chem. Phys. **201**, 147–155 (2017)
36. Y. Qingbo, K. Yang, H. Li, X. Li, Z-scheme α-Fe2O3/g-C3N4 with the FeOC bond toward enhanced photocatalytic degradation. Colloids Surf., A **616**, 126269 (2021)
37. L. You, M. Gao, T. Li, L. Guo, P. Chen, M. Liu, Investigation of the kinetics and mechanism of Z-scheme Ag 3 PO 4/WO 3 p–n junction photocatalysts with enhanced removal efficiency for RhB. New J. Chem. **43**, 17104–17115 (2019)